Scripta Materialia 275 (2026) 117178

Contents lists available at ScienceDirect

Scripta Materialia

journal homepage: www.journals.elsevier.com/scripta-materialia

The role of grain size distribution on the anomalous yielding of ultrafine-grained Au thin films

Yichen Yang [a], Kunqing Ding [a], Ting Zhu [a], Josh Kacher [b], Olivier Pierron [a,*]

[a] Woodruff School of Mechanical Engineering, Georgia Institute of Technology, Atlanta, GA 30332, USA
[b] School of Materials Science and Engineering, Georgia Institute of Technology, Atlanta, GA 30332, USA

ARTICLE INFO

Keywords:
Ultrafine grained thin films
Grain boundary migration
In situ TEM
Yield stress

ABSTRACT

Ultrafine grained metals, with grain size ranging from 100 nm to 1 μm, generally exhibit increasing strength with decreasing grain size, as expected by the Hall-Petch relationship. Contrary to this trend, we observe an increase in yield strength from 310 to 520 MPa as the average grain size of Au thin films increases from 140 to 360 nm after annealing at 350 °C. Quantitative in situ TEM nanomechanical testing reveals that the grain size distribution plays a key role in determining the films' yield strength. In the as-deposited state, a large area fraction of nanograins (<50 nm in size) adjacent to larger grains results in substantial stress-assisted grain-boundary migration and grain coalescence, leading to yielding at relatively low applied stresses. When these small grains are removed through annealing, grain boundary migration is largely suppressed, and higher stresses are required to initiate dislocation-mediated yielding, despite the coarser average grain size.

Nanocrystalline (NC) and ultrafine grained (UFG) metals constitute an important class of materials due to their high strength [1–3]. As the grain size decreases, transgranular dislocation activity is increasingly confined [4–6], leading to a rise in strength, as predicted by the Hall–Petch relationship [7,8]. However, grain boundaries (GBs) possess excess free volume and disordered atomic structures, which limit their thermal or mechanical stability in this grain size regime [9]. Such instability can induce stress-assisted GB migration (GBM), resulting in grain coarsening and a concomitant reduction in strength [10–17]. At sufficiently small grain sizes (typically $\lesssim$10–20 nm), Hall–Petch strengthening can break down and even invert (inverse Hall–Petch), as plastic strain is increasingly accommodated by GB sliding with diffusion-assisted accommodation [7,18]. Two complementary strategies have been proposed to enhance GB stability. The first strategy provides stabilization against grain coarsening through both thermodynamic and kinetic effects—solute segregation at GBs lowers the interfacial free energy and increases the coarsening barrier, while Zener pinning mechanically restrains boundary motion [19–22]. The second strategy is based on structural stabilization by relaxing nonequilibrium GBs toward lower-energy, more ordered configurations (including equilibrium complexion states) [23]. Hasnaoui et al. [24] investigated the structural order of GB and triple junctions (TJ) from annealing via atomistic simulations and demonstrated that atomic shuffling and migration during annealing allows GBs and TJs to reach a more equilibrium geometry. Recent evidence further confirms that appreciable grain growth can be effectively suppressed via short-term thermal treatments. Hu et al. [2] reported a slight increase in strength (about 15 %) from ~4.3 to ~4.9 GPa in NC Ni by relaxing the GB structure through annealing at a temperature below 200 °C for 1 hour, without any significant change in the average grain size. This annealing-induced strengthening is thought to be mainly due to GB stabilization.

In this work, we report a ~70 % increase in yield strength after annealing 100-nm-thick UFG Au thin films. This result is counterintuitive given the concurrent ~2 × increase in average grain size, i.e., an apparent inverse Hall–Petch–like trend is observed even though the grain sizes remain well above the NC regime where classic Hall–Petch breakdown is typically reported. To elucidate the underlying mechanism, we employ quantitative in situ transmission electron microscopy (TEM) mechanical testing to investigate the influence of grain size distribution and GB stability under mechanical loading on the resulting yield strength [12,25–28].

Dog-bone-shaped, 100-nm-thick Au film microspecimens (with width of ~1.5 μm and length of ~10 μm) were fabricated using e-beam evaporation [25,27,28]. A subset of specimens, denoted as A350 and A700, was annealed at 350 °C for 30 min and 700 °C for 5 min, under a pressure of 10^{-5} Torr. In situ TEM tensile experiments of the Au

* Corresponding author at: Georgia Institute of Technology Atlanta, Ga, USA.
E-mail address: olivier.pierron@me.gatech.edu (O. Pierron).

https://doi.org/10.1016/j.scriptamat.2026.117178
Received 20 October 2025; Received in revised form 5 January 2026; Accepted 9 January 2026

microspecimens were carried out with our custom-developed micro-electromechanical system (MEMS) testing platform [25,27–29]. Microstructural characterization was performed using a Gatan OneView detector in a ThermoFisher Tecnai F30 transmission electron microscope (TEM) operated at an accelerating voltage of 300 kV with bright-field imaging. Specimens were mechanically loaded to the onset of yielding and then let to relax for 2–5 min for in situ TEM observations. The dislocation density ρ was quantified by manually tracing dislocations using ImageJ software. The total dislocation length (L_{total}) within the observed field of view was determined by summing the traced lengths, using the relation $\rho = \frac{L_{\text{total}}}{V_{\text{sample}}}$, where V_{sample} represents the sampled volume, calculated as the product of the field of view area and the thickness of the TEM specimen (100 nm). Since only dislocations with $\mathbf{g}\cdot\mathbf{b} \neq 0$ are visible in bright-field imaging, raw counts were scaled by a factor of 3 to account for (i) invisibility and (ii) 2-D projection, assuming an average 45° inclination of dislocation lines to the foil normal, in line with standard practice performed by other dislocation density measurements [30,31]. Although this correction factor introduces an overall change, it is consistent across all specimens and

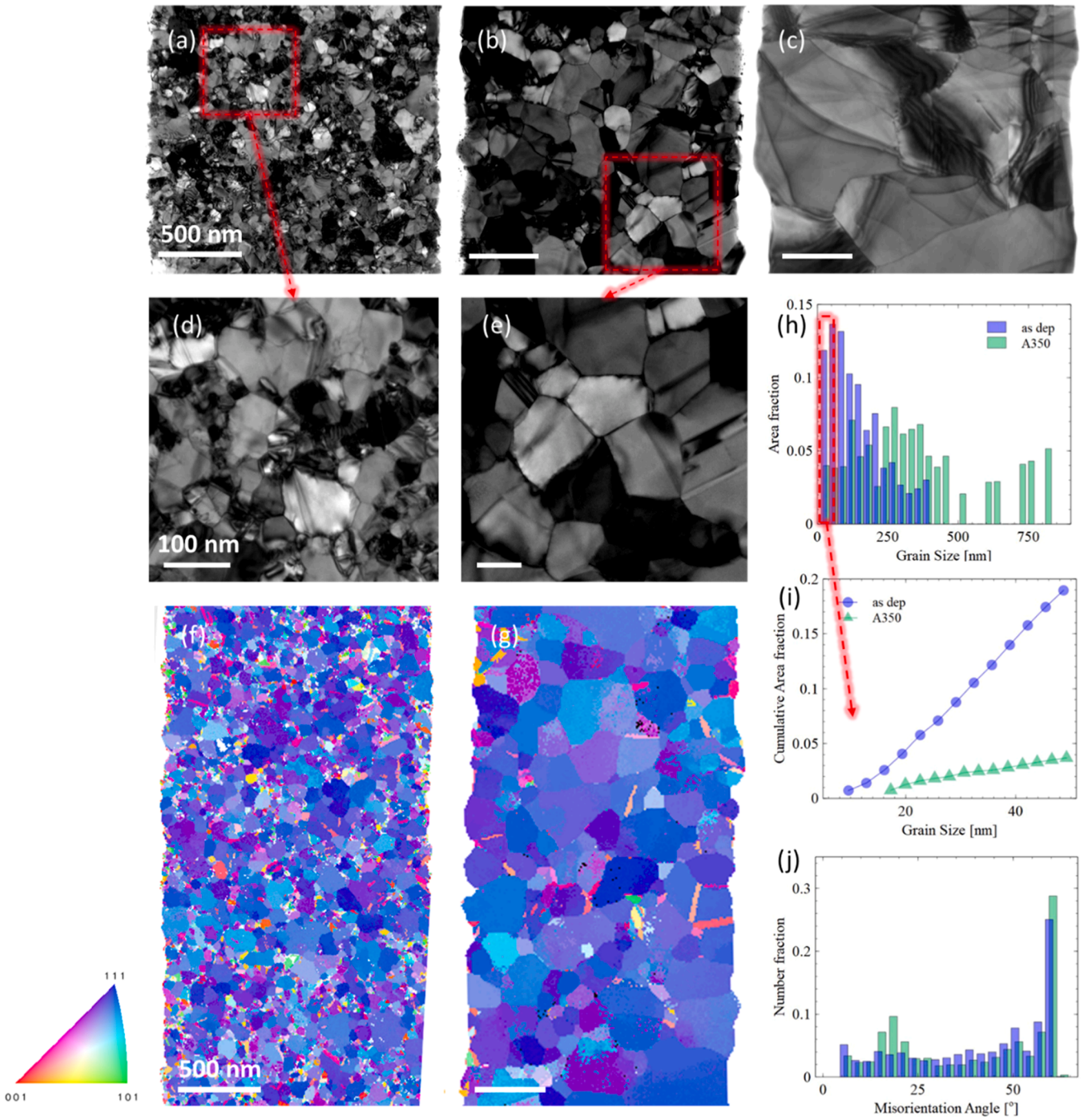

Fig. 1. Bright field (BF) TEM images of the initial microstructure of the (a) as-deposited, (b) A350, and (c) A700 specimens. (d-e) High magnification BF images of the cropped regions in (a) and (b), respectively. PED maps of (e) as-deposited and (f) A350 annealed specimen. (h) Grain size distribution acquired from PED datasets. (i) Cumulative area fraction of grains below 50 nm within the distribution of grain size taken from the PED data. (j) GB misorientation distribution plots taken from the PED data.

therefore does not compromise the relative comparison discussed herein. Precession electron diffraction (PED) was conducted using a Thermo Fisher Tecnai F20 TEM operated at 200 kV at the University of Alabama using a side mounted Stingray camera from Nanomegas and a precession angle of 0.5 ° [12]. The scan step size was set to ~1/20 of the average grain size (typically 5–10 nm), and 2–3 precession conditions were acquired depending on grain size. Orientation datasets were indexed and analyzed in Orientation Imaging Microscopy (OIM) software.

Fig. 1 (a-c) shows bright field TEM images of the initial microstructures for the as-deposited, A350 and A700 conditions, respectively. Higher-magnification images of the as-deposited and A350 films are shown in Fig. 1(d, e). Two inverse pole figure (IPF) maps are shown in Fig. 1(f) and (g) for the as-deposited and A350 conditions, respectively, showing a strong ⟨111⟩ out-of-plane texture. The corresponding grain size distributions are shown in Fig. 1(h), with area-weighted average grain sizes (defined by their equivalent diameters d_m) of 142±36 and 360±83 nm for the as-deposited and A350 specimens, respectively. Grains smaller than 50 nm occupy 20 % of the total area of the as-deposited specimen, whereas they only occupy 3 % for the A350 specimen (Fig. 1(i)). Although most of the grains exhibit columnar structures, grains smaller than 50 nm can be stacked through the thickness. A closer view of this mixed grain structure for the as-deposited condition is shown in the high magnification inset (Fig. 1 (d)), where a few larger grains (usually with a strong ⟨111⟩ texture, shown in Fig. 1(f)) are interspersed with numerous smaller, randomly oriented grains. For the A700 specimen (Fig. 1(c)), only a few grains span the specimen width, and the limited grain count precludes a statistically meaningful distribution analysis. However, the d_m was approximated to ~770 nm based on the TEM images. The misorientation data (Fig. 1(j)) reveals that both the as-deposited and A350 specimens have similar GB misorientation angle distributions, with a slightly larger number of Σ3 twin boundaries observed after annealing. The measured dislocation densities are 5.4 × 10^{14} m^{-2} for the as-deposited sample, 5.1 × 10^{14} m^{-2} for the A350 sample, and 2.7 × 10^{13} m^{-2} for the A700 sample.

Fig. 2 shows representative stress-strain curves for the three initial microstructures tested at two different strain rates $\dot{\varepsilon}$ (~10^{-4} s^{-1} and ~10^{-1} s^{-1}). Two tests were repeated at 10^{-4} s^{-1} to confirm reproducibility. At $\dot{\varepsilon}$ ~ 10^{-4} s^{-1}, the as-deposited specimens exhibit a 0.2 % offset yield stress (σ_y) of 312±3 MPa, whereas σ_y = 530±10 MPa and 467±3 MPa for the A350 and A700 specimens, respectively. At $\dot{\varepsilon}$ ~

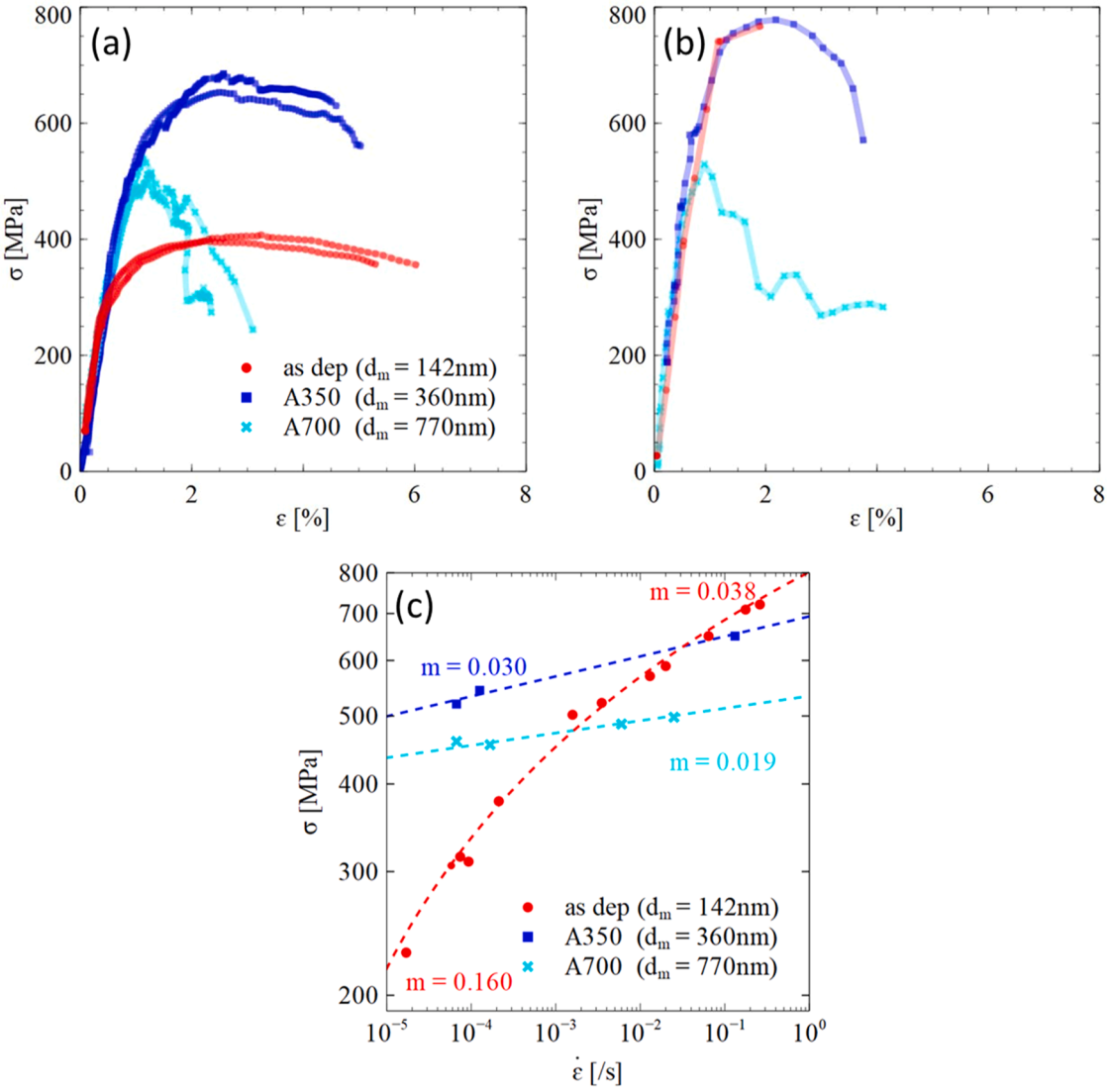

Fig. 2. Stress-strain relationship of as-deposited and annealed specimens under applied strain rates of (a) 10^{-4} s^{-1} and (b) 10^{-1} s^{-1}. (c) Yield stress vs strain rate for the three conditions and their strain rate sensitivity. The as-deposited data were fitted using a logarithmic relation, while the A350 and A700 data were fitted using power-law relations.

10^{-1} s^{-1}, the as-deposited specimen exhibits a σ_y of 659 MPa, slightly higher than the σ_y of 650 MPa for A350, and significantly higher than that of the A700 sample (482 MPa). Additional tests were performed at applied strain rates between $\sim 10^{-5}$ and $\sim 10^{-1}$ s^{-1} to obtain the strain rate sensitivity factor m for the three conditions. As shown in Fig. 2(c), $m = 0.030$ and 0.019 for the A350 and A700 specimens, respectively, and is constant across the studied range of $\dot{\varepsilon}$. In contrast, the strain-rate sensitivity of the as-deposited film cannot be adequately described by a single power-law relation, as the slope of the $\sigma_y - \dot{\varepsilon}$ curve changes continuously over the measured range. Therefore, a logarithmic fit was employed to capture this gradual variation. Two distinct regimes can be identified from the curvature of the fit: a low-strain-rate regime ($< 10^{-3}$ s^{-1}) where m increases sharply, and a high-strain-rate regime ($> 10^{-3}$ s^{-1}) where m remains relatively constant. Specifically, under the higher strain rate conditions ($\dot{\varepsilon} \sim 10^{-3}$ s^{-1} in Fig. 2(c)), σ_y decreases with increasing d_m, as qualitatively expected based on the Hall-Petch relationship. In the low strain rate regime, at $\dot{\varepsilon} \sim 10^{-4}$ s^{-1}, σ_y increases as d_m increases from 140 to 360 nm but decreases with further increasing d_m from 360 to 770 nm. The disparity in m across the different conditions and applied strain rates suggests a variation of deformation processes, motivating in situ TEM observations below.

Fig. 3 illustrates the deformation behavior during stress relaxation in an as-deposited sample loaded to 335 MPa at 10^{-4} s^{-1} (slightly above the yield stress). The observations start within the first 5 s of the onset of relaxation and are tracked over the duration of 2 min; see also Supplementary Movie S1. At the onset of relaxation, rapid GBM was observed: a large grain (labeled '1′ in Fig. 3a) grew at the expense of a smaller neighboring grain (30 nm, labelled '2′ in Fig. 3a), leading to Grain 2

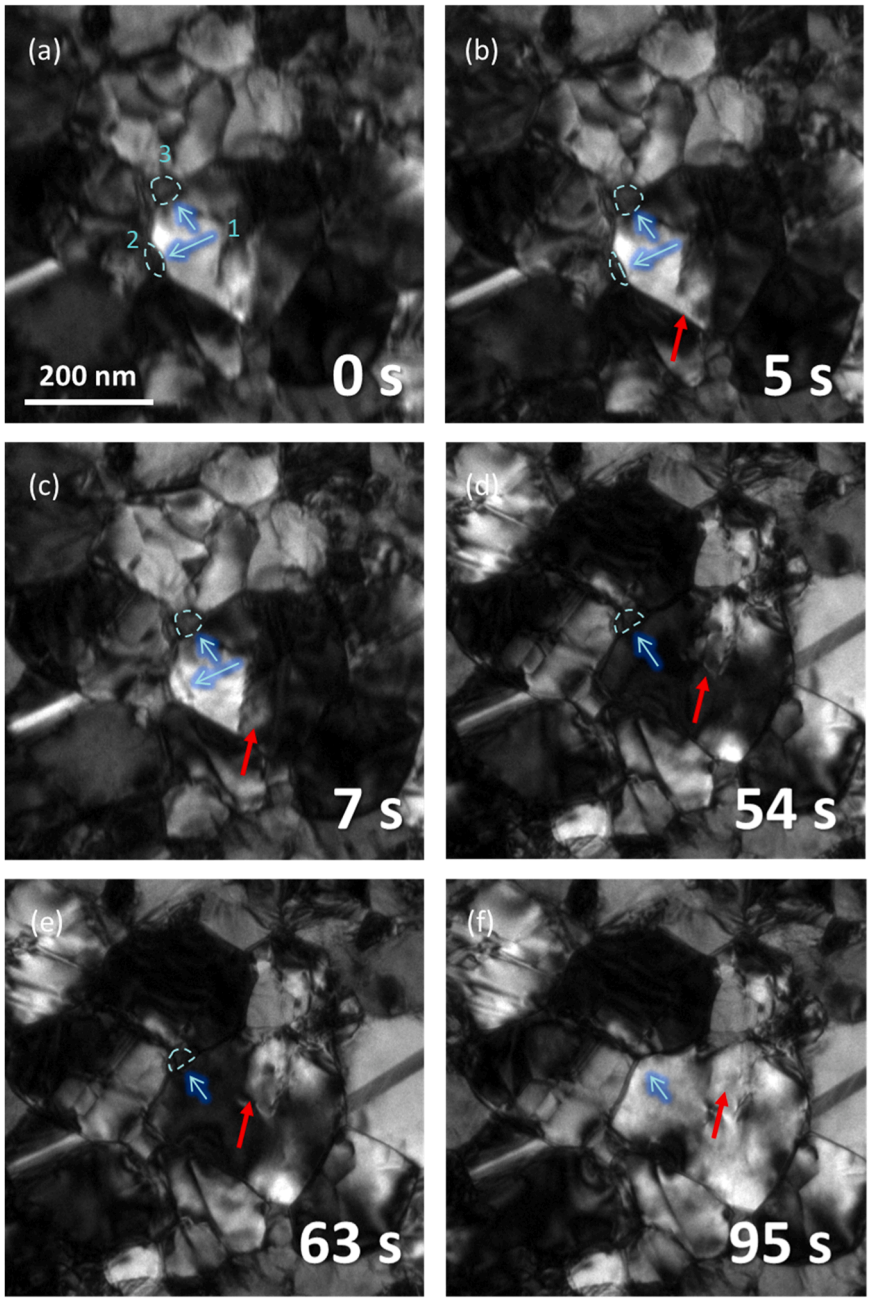

Fig. 3. Snapshots from an in situ TEM video showing the stress relaxation of the as-deposited specimen after loading to 335 MPa, demonstrating rapid stress assisted GBM with coarsening. The outlined grains are numbered 1, 2, and 3 for reference in the text and the blue arrows indicate the direction of GBM. The red arrow tracks a single dislocation.

completely disappearing within 7 s. Contrast changes in bright field images suggest a lattice rotation event toward the orientation of the growing grain. Simultaneously, intragranular dislocation activity was observed, as indicated by the red arrow tracking its position in Fig. 3 (b-f). Intragranular dislocation activity was restricted to Grain 1, while the surrounding smaller grains exhibited no visible activity throughout the observed sequence. The process of large grains growing at the expense of small grains continued over the course of the relaxation, with a second example highlighted in Fig. 3 (e-f). Here, a grain with initial diameter of 40 nm (labeled '3' in Fig. 3a), began to shrink at 54 s and vanished by 95 s.

Fig. 4 depicts TEM observations during relaxation of an A350 specimen, also shown in Supplementary Movie S2. The sample was loaded to ~550 MPa (right above its yield stress) at 10^{-4} s^{-1}. At the onset of relaxation, extensive transgranular dislocation activity was observed, including dislocation nucleation, pile-up formation, and slip transmission across GBs. Dislocation-GB intersections are marked by red triangles and distinct slip bands are indicated by colored arrows in Fig. 4. The GB network remained mostly stable under applied stress, with no grains undergoing complete annihilation. Unlike the dislocation activity in the as-deposited specimen, where dislocation glide was restricted to single slip systems within each grain, dislocations were observed gliding on multiple slip systems with dislocation cross-slip occurring (shown in Fig. 4(b)). For comparison, another experiment was conducted to load the A350 specimen to only 350 MPa (i.e. elastic regime for A350)—the yield stress of the as-deposited condition—no plastic activity (dislocation motion or GBM) was detected, and the corresponding data is therefore not shown.

The above results demonstrate that at low strain rates (~10^{-4} s^{-1}), we observe an anomalous strengthening behavior. Despite an increase in

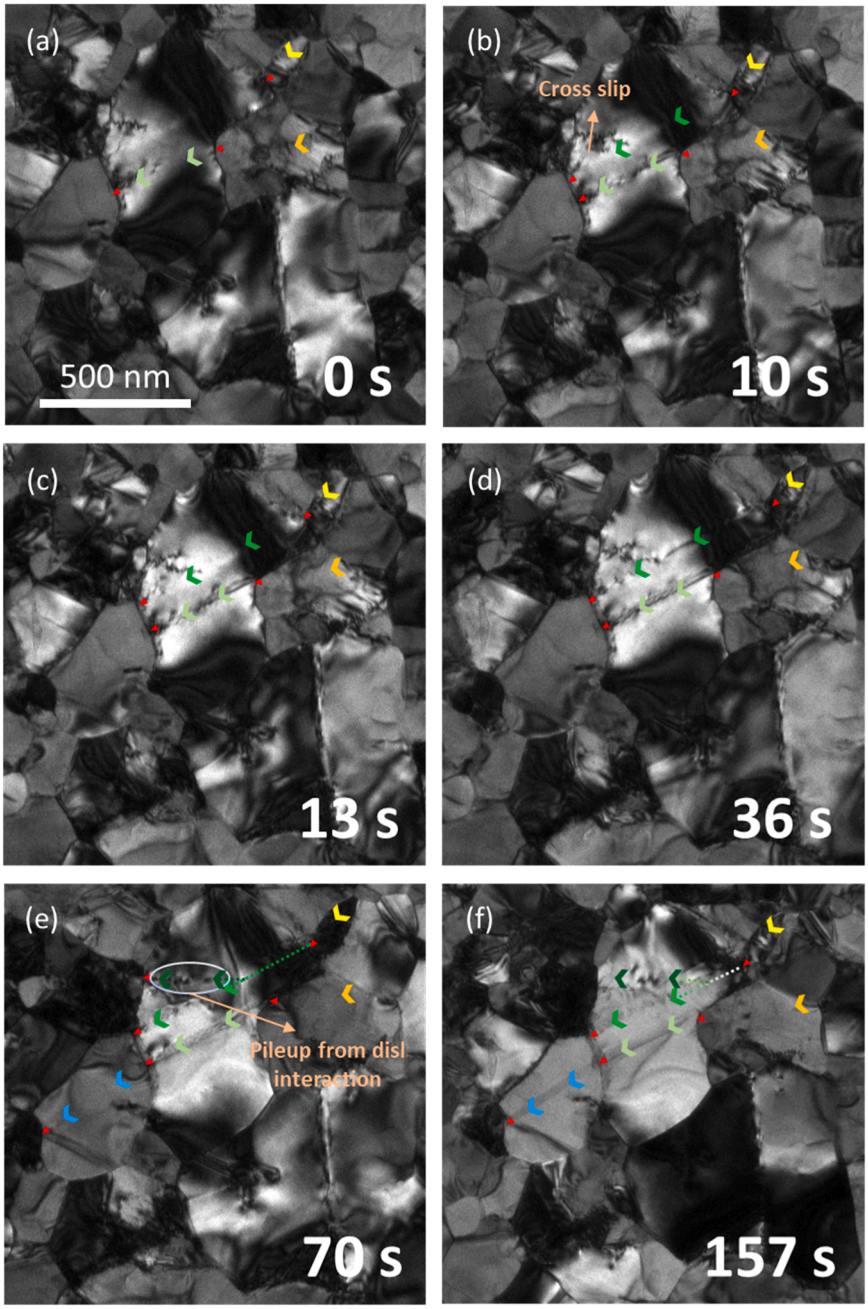

Fig. 4. Snapshots from an in situ TEM video showing relaxation of A350 after loading to 550 MPa. The red triangles indicate dislocation pile-ups at GBs. Arrows with different colors represent different slip bands. The time from the onset of observation is given in each frame.

the average grain size from ~142 nm in the as-deposited state to ~360 nm in the annealed A350 condition, the yield strength increases from ~310 MPa to ~520 MPa. Notably, the grain sizes are well above the NC regime (< ~10–20 nm) where inverse Hall–Petch behavior is generally observed [7,32]. In contrast, at higher strain rates (~10^{-1} s^{-1}), where the experimental time scale suppresses significant GBM, the yield strengths seem to recover the Hall–Petch relation (see Fig. 2(c)). It is necessary to note that although the electron beam in TEM can, at lower strain rate, accelerate deformation processes through beam-induced bombardment, its influence on Au is negligible [27]. Therefore, the observed mechanical response is intrinsic to the material and unaffected by electron-beam irradiation, ensuring the reliability of the in situ TEM measurements.

Previous studies have shown that annealing-induced reductions in mobile dislocation density can increase σ_y in UFG metals [33,34]. However, the as-deposited and A350 films show nearly identical initial dislocation densities (5.4×10^{14} vs. 5.1×10^{14} m^{-2}, respectively), indicating that differences in the dislocation state cannot account for the observed anomalous strengthening.

There is considerable experimental and computational evidence in the literature [2,14,35–37] demonstrating that GBM significantly influences σ_y of NC and UFG metals. The higher σ_y of the A350 film at low strain rate is primarily attributed to enhanced GB stability following annealing. First, annealing removes high-energy, nonequilibrium GBs and preexisting disconnections with finite step components, resulting in a more stable boundary network that resists stress-induced GBM. Second, the process relieves residual stresses—particularly pronounced in smaller grains—that otherwise promote GBM and grain coalescence. Third, annealing eliminates facile migration pathways that enable stress-assisted grain growth in the as-deposited film. However, the pronounced strengthening observed here suggests additional mechanisms beyond enhanced GB stability as discussed earlier. Prior studies on NC Ni have shown that GB mobility decreases markedly after 1 h of annealing at 200 °C, resulting in ~15 % increase in yield strength without any measurable grain coarsening [2]. The extent of relaxation can be further amplified depending on boundary state and chemistry (e.g., higher purity Cu exhibits greater annealing-induced stability [38]). In addition to structural relaxation, annealing may also modify GB mobility through impurity redistribution and segregation (e.g., solute drag), which could in turn affect strength. The high-purity Au feedstock (99.995 %) and high-vacuum deposition/annealing minimizes the likelihood of substantial impurity uptake. Consistently, TEM–EDS shows no detectable impurity enrichment at GBs within our measurement sensitivity (i.e., no segregant signal above the typical sub-wt % level for heavy elements). Nonetheless, ppm-level redistribution cannot be fully excluded and could further reduces GB mobility [39].

A second, readily apparent microstructural change is the marked reduction in the sub-50 nm population after annealing (Fig. 1i). Removing these sub-50-nm grains suppresses stress-assisted GBM and diminishes the associated GB-mediated dislocation-emission sites On one hand, homogenization of the grain size distribution after annealing substantially reduces the driving force for GBM. According to the Hall–Petch relation, smaller grains require higher stresses for yielding than larger ones, creating gradients of stress and strain energy density across boundaries separating grains of different sizes. These gradients act as a driving force for GBM and become more pronounced with broader grain-size distributions [40]. This explains the rapid GBM observed in the as-deposited films, where large grains grow at the expense of small ones (Fig. 3), and the limited plasticity observed in the larger grains of the A350 film under the same applied stress level. On the other hand, annealing removes easy dislocation sources, thereby increasing the critical stress for dislocation nucleation. In contrast, the high GB mobility in the as-deposited film facilitates local atomic shuffling and stress-assisted free-volume migration [33,37], effectively lowering the barrier for dislocation nucleation. Recent experiments and molecular dynamics simulations by Liu et al. [37] also showed that stress-driven grain growth promotes dislocation emission and enhances ductility, consistent with our observations of concurrent GB migration and nearby dislocation emission in the as-deposited film at only ~350 MPa. The A350 films exhibit a significant reduction in sub 50 nm grains after annealing (decreasing from 20 % area fraction in the as-deposited state to 3 % after annealing; see Fig. 1(i)), which hinders GBM and therefore removes GB dislocation emission sources. These results are consistent with previous work on Al thin films, where stress-assisted grain growth was found to strongly influence σ_y [14]: σ_y was ~290 MPa in the absence of stress-assisted grain growth, but only ~120 MPa when stress-assisted grain growth occurred. In that study, the absence of stress-assisted grain growth was attributed to impurities (whose level depended on the deposition conditions) [35]. We therefore attribute the 70 % increase in σ_y despite grain coarsening to the suppression of stress-assisted GBM due to combined effect of narrowing of the grain-size distribution and reduced GB mobility after annealing, although our data do not uniquely separate the relative contributions of these two effects.

It should be noted that the above discussion focuses on the as-deposited and A350 films. The reduced ductility and minimal post-yield hardening observed in the A700 specimen is likely geometric in origin, as only one to two grains span the specimen width. Local stress concentrations may arise from grain boundary dihedral intersections and surface roughness along the gauge edges, and the substantially lower initial dislocation density (2.7×10^{13} m^{-2}) may further reduce work hardening. However, the measured yield strength remains a valid basis for comparison.

To summarize, annealing UFG Au thin films leads to a significant increase in σ_y and decrease in strain rate sensitivity variability. Microstructurally, annealing promotes overall grain coarsening, primarily through the elimination of sub-50 nm grains. In situ TEM observations reveal that in the as-deposited films, grain coarsening initiates almost immediately upon yielding, underscoring a strong correlation between GB stability and the deformation behavior. After annealing, GBs are more stable and the sub-50 nm grains are almost entirely removed from the microstructure, thereby suppressing GBM as a low-stress deformation mechanism. Consequently, yielding occurs at higher stresses despite the larger average grain size. The contrast in yielding behavior between the two microstructures diminishes at higher strain rates, reflecting the strain-rate dependence of GBM. These findings highlight the critical role of the fine-grain tail of the size distribution in governing the mechanical response of UFG thin films.

Declaration of generative AI and AI-assisted technologies in the manuscript preparation process

During the preparation of this work the author(s) used ChatGPT in order to reduce wordcount and streamline phrasing. After using this tool/service, the authors reviewed and edited the content as needed and take full responsibility for the content of the published article.

CRediT authorship contribution statement

Yichen Yang: Writing – original draft, Investigation, Formal analysis, Data curation. **Kunqing Ding:** Writing – review & editing, Formal analysis. **Ting Zhu:** Writing – review & editing, Supervision, Funding acquisition, Formal analysis, Data curation. **Josh Kacher:** Writing – review & editing, Supervision, Funding acquisition, Formal analysis, Data curation. **Olivier Pierron:** Writing – review & editing, Supervision, Funding acquisition, Formal analysis, Conceptualization.

Declaration of competing interest

The authors declare that they have no known competing financial interests or personal relationships that could have appeared to influence the work reported in this paper.

Acknowledgments

The authors gratefully acknowledge support by the U.S. Department of Energy (DOE), Office of Science, Basic Energy Sciences (BES) Materials Science and Engineering (MSE) Division under Award #DE-SC0018960. The authors also thank Sandra Stangebye for her assistance in collecting the PED orientation maps.

Supplementary materials

Supplementary material associated with this article can be found, in the online version, at doi:10.1016/j.scriptamat.2026.117178.

References

[1] R.Z. Valiev, I.V. Alexandrov, M. Kawasaki, T.G. Langdon, Ultrafine-grained materials, in: R.Z. Valiev, I.V. Alexandrov, M. Kawasaki, T.G. Langdon (Eds.), Ultrafine-Grained Materials, Springer International Publishing, Cham, 2024, pp. 1–29.
[2] J. Hu, Y.N. Shi, X. Sauvage, G. Sha, K. Lu, Grain boundary stability governs hardening and softening in extremely fine nanograined metals, Science 355 (6331) (2017) 1292–1296.
[3] O. Renk, V. Maier-Kiener, I. Issa, J.H. Li, D. Kiener, R. Pippan, Anneal hardening and elevated temperature strain rate sensitivity of nanostructured metals: their relation to intergranular dislocation accommodation, Acta Mater. 165 (2019) 409–419.
[4] H. Conrad, Grain size dependence of the plastic deformation kinetics in Cu, Mater. Sci. Eng. a-Struct. Mater. Prop. Microstruct. Process. 341 (1–2) (2003) 216–228.
[5] H. Conrad, Plastic deformation kinetics in nanocrystalline FCC metals based on the pile-up of dislocations, Nanotechnology. 18 (32) (2007) 325701.
[6] S. Cheng, J.A. Spencer, W.W. Milligan, Strength and tension/compression asymmetry in nanostructured and ultrafine-grain metals, Acta Mater. 51 (15) (2003) 4505–4518.
[7] C.E. Carlton, P.J. Ferreira, What is behind the inverse Hall–Petch effect in nanocrystalline materials? Acta Mater. 55 (11) (2007) 3749–3756.
[8] H. Conrad, J. Narayan, On the grain size softening in nanocrystalline materials, Scr. Mater. 42 (11) (2000) 1025–1030.
[9] T. Chookajorn, H.A. Murdoch, C.A. Schuh, Design of stable nanocrystalline alloys, Science 337 (6097) (2012) 951–954.
[10] S. Kobayashi, A. Kamata, T. Watanabe, A mechanism of grain growth-assisted intergranular fatigue fracture in electrodeposited nanocrystalline nickel–phosphorus alloy, Acta Mater. 91 (2015) 70–82.
[11] M. Legros, D.S. Gianola, K.J. Hemker, In situ TEM observations of fast grain-boundary motion in stressed nanocrystalline aluminum films, Acta Mater. 56 (14) (2008) 3380–3393.
[12] S. Stangebye, K. Ding, Y. Yang, T. Zhu, O. Pierron, J. Kacher, Grain size effects on stress-assisted grain boundary migration in polycrystalline Au thin films under tension, Acta Mater. 297 (2025) 121330.
[13] T.J. Rupert, D.S. Gianola, Y. Gan, K.J. Hemker, Experimental observations of stress-driven grain boundary migration, Science 326 (5960) (2009) 1686–1690.
[14] D.S. Gianola, S. Van Petegem, M. Legros, S. Brandstetter, H. Van Swygenhoven, K. J. Hemker, Stress-assisted discontinuous grain growth and its effect on the deformation behavior of nanocrystalline aluminum thin films, Acta Mater. 54 (8) (2006) 2253–2263.
[15] P. Baral, A. Kashiwar, M. Coulombier, L. Delannay, K. Hoummada, J.P. Raskin, H. Idrissi, T. Pardoen, Grain boundary-mediated plasticity in aluminum films unraveled by a statistical approach combining nano-DIC and ACOM-TEM, Acta Mater. 276 (2024).
[16] H. Idrissi, A. Kobler, B. Amin-Ahmadi, M. Coulombier, M. Galceran, J.P. Raskin, S. Godet, C. Kubel, T. Pardoen, D. Schryvers, Plasticity mechanisms in ultrafine grained freestanding aluminum thin films revealed by in-situ transmission electron microscopy nanomechanical testing, Appl. Phys. Let 104 (10) (2014) 5.
[17] F. Mompiou, M. Legros, A. Boe, M. Coulombier, J.P. Raskin, T. Pardoen, Inter- and intragranular plasticity mechanisms in ultrafine-grained Al thin films: an in situ TEM study, Acta Mater. 61 (1) (2013) 205–216.
[18] J. Kong, M.J.R. Haché, J. Tam, J.L. McCrea, J. Howe, U. Erb, On the extrinsic Hall-petch to inverse Hall-Petch transition in nanocrystalline Ni-Co electrodeposits, Scr. Mater. 218 (2022) 114799.
[19] S.V. Sevlikar, G.M. Muralikrishna, D. Gaertner, S. Starikov, T. Brink, D. Scheiber, D. Smirnova, D. Irmer, B. Tas, V.A. Esin, V.I. Razumovskiy, C.H. Liebscher, G. Wilde, S.V. Divinski, Grain boundary diffusion and segregation of Cr in Ni Σ11 (1¯13)[110]bicrystals: decoding the role of grain boundary defects, Acta Mater. 278 (2024) 120229.
[20] N.M. Heckman, A. Barrios, C.M. Barr, D.P. Adams, T.A. Furnish, K. Hattar, B. L. Boyce, Solute segregation improves the high-cycle fatigue resistance of nanocrystalline Pt-Au, Acta Mater. 229 (2022) 117794.
[21] S. Tang, Z. Zhang, Q. Cai, Y. Ma, W. Liu, The atomic scale mechanisms of the interaction between pore and grain boundary during sintering, Mater. Today Commun. 32 (2022) 103970.
[22] D.S. Gianola, D. Farkas, M. Gamarra, M.-r. He, The role of confinement on stress-driven grain boundary motion in nanocrystalline aluminum thin films, J. Appl. Phys 112 (12) (2012) 124313.
[23] C.A. Schuh, K. Lu, Stability of nanocrystalline metals: the role of grain-boundary chemistry and structure, MRS Bull. 46 (3) (2021) 225–235.
[24] A. Hasnaoui, H. Van Swygenhoven, P.M. Derlet, On non-equilibrium grain boundaries and their effect on thermal and mechanical behaviour: a molecular dynamics computer simulation, Acta Mater. 50 (15) (2002) 3927–3939.
[25] S. Gupta, S. Stangebye, K. Jungjohann, B. Boyce, T. Zhu, J. Kacher, O.N. Pierron, In situ TEM measurement of activation volume in ultrafine grained gold, Nanoscale 12 (13) (2020) 7146–7158.
[26] S. Stangebye, K. Ding, Y. Zhang, E. Lang, K. Hattar, T. Zhu, J. Kacher, O. Pierron, Direct observation of grain-boundary-migration-assisted radiation damage healing in ultrafine grained gold under mechanical stress, Nano Lett. 23 (8) (2023) 3282–3290.
[27] S. Stangebye, Y. Zhang, S. Gupta, T. Zhu, O. Pierron, J. Kacher, Understanding and quantifying electron beam effects during in situ TEM nanomechanical tensile testing on metal thin films, Acta Mater. 222 (2022) 117441.
[28] S. Stangebye, X. Liu, L. Daza Llanos, Y. Yang, T. Zhu, J. Kacher, O. Pierron, Comparison of electrical sensing and image analysis for in situ transmission electron microscopy nanomechanical testing of thin films, Thin. Solid. Films. 787 (2023) 140125.
[29] Y. Yang, K. Ding, X. Liu, T. Zhu, J. Kacher, O. Pierron, In-situ TEM measurement of strain-rate-dependent activation volume in ultrafine grained gold films, Acta Mater. 306 (2026) 121868.
[30] K. Bawane, X. Liu, T. Yao, M. Khafizov, A. French, J.M. Mann, L. Shao, J. Gan, D. H. Hurley, L. He, TEM characterization of dislocation loops in proton irradiated single crystal ThO2, J. Nucl. Mater. 552 (2021) 152998.
[31] D. Kiener, A.M. Minor, Source truncation and exhaustion: insights from quantitative in situ TEM tensile testing, Nano Lett. 11 (9) (2011) 3816–3820.
[32] H. Zhang, F. Liu, G. Ungar, Z. Zheng, Q. Sun, Y. Han, A regime beyond the Hall–Petch and inverse-Hall–Petch regimes in ultrafine-grained solids, Commun. Phys. 5 (1) (2022) 329.
[33] Y.M. Wang, A.V. Hamza, E. Ma, Activation volume and density of mobile dislocations in plastically deforming nanocrystalline Ni, Appl. Phys. Let 86 (24) (2005).
[34] E.-A. Choi, Y.S. Lee, S.J. Lee, J.H. Ahn, S.H. Lim, S. Semboshi, S.Z. Han, Strengthening effect of decreased dislocation density after annealing in pure aluminum or copper, Met. Mater. Int. 30 (3) (2024) 607–617.
[35] D.S. Gianola, D.H. Warner, J.F. Molinari, K.J. Hemker, Increased strain rate sensitivity due to stress-coupled grain growth in nanocrystalline Al, Scr. Mater. 55 (7) (2006) 649–652.
[36] Y. Zhang, G.J. Tucker, J.R. Trelewicz, Stress-assisted grain growth in nanocrystalline metals: grain boundary mediated mechanisms and stabilization through alloying, Acta Mater. 131 (2017) 39–47.
[37] C. Liu, W. Lu, G.J. Weng, J. Li, A cooperative nano-grain rotation and grain-boundary migration mechanism for enhanced dislocation emission and tensile ductility in nanocrystalline materials, Mater. Sci. Eng.: A 756 (2019) 284–290.
[38] H. Fu, X. Zhou, H. Xue, X. Li, K. Lu, Breaking the purity-stability dilemma in pure Cu with grain boundary relaxation, Mater. Today 55 (2022) 66–73.
[39] D. Scheiber, Segregation and embrittlement of gold grain boundaries, Comput. Mater. Sci. 187 (2021) 110110.
[40] T. Morita, R. Mitra, J.R. Weertman, Micromechanics model concerning yield behavior of nanocrystalline materials, Mater. Trans. 45 (2) (2004) 502–508.